High-Efficiency and High-Precision Reconstruction Strategy for P-Band Ultra-Wideband Bistatic Synthetic Aperture Radar Raw Data Including Motion Errors

HONGTU XIE[1,2], (Member, IEEE), JUN HU[1], (Member, IEEE), KEQING DUAN[1], (Member, IEEE), AND GUOQIAN WANG[3]

[1]School of Electronics and Communication Engineering, Sun Yat-sen University, Guangzhou 510006, China
[2]College of Electronic Science, National University of Defense Technology, Changsha 410073, China
[3]Sun Yat-sen Memorial Hospital, Sun Yat-sen University, Guangzhou 510120, China

Corresponding authors: Guoqian Wang (30134537@qq.com) and Jun Hu (348158489@qq.com)

ABSTRACT P-band ultra-wideband bistatic synthetic aperture radar (UWB BSAR) has the well capability of the foliage penetrating, high-resolution imaging and adding the scattered information, which is potential of detecting the concealed target. However, the P-band UWB BSAR raw data is of the huge amount, big spatial-variance, significant range azimuth coupling and complicated motion error, which increases the difficulty of the efficient and precise reconstruction. In this paper, we propose a reconstruction strategy for the P-band UWB BSAR raw data including the motion errors, which can solve the above problems with the high-efficiency and high-precision. This method requires the local beamforming from the raw data as an intermediate processing in the slant range plane instead of ground plane, which can be exactly referenced to the tracks of the transmitter and receiver considering platform altitudes. And, it derives the requirement for selecting the subapertures and subimages by analyzing the bistatic range error considering the motion errors, as well as sampling requirement of the beam for the subimages, which offers a near-optimum tradeoff between the precision and efficiency. Simulated and measured results show that the proposed strategy is effective, and can achieve the near optimal performance with the low computational complexity.

INDEX TERMS Bistatic synthetic aperture radar (BSAR), fast factorized backprojection (FFBP), high-efficiency and high-precision reconstruction, motion errors, P-band ultra-wideband.

I. INTRODUCTION

With the rapid development of the remote sensing techniques [1]–[7], the huge amount of the remote sensing data has been acquired from the sensor platforms such as the satellites and aircrafts [8], [9], complemented by the surface and subsurface measurements and mapping [10], [11]. The remote sensing data is useful for the inventarisation and management of the natural resources (such as the

The associate editor coordinating the review of this manuscript and approving it for publication was Wei Wang.

agricultural land, forests, soils, mineral deposits and water resources) [12]–[16] and the environment (such as the industrial pollution, biodiversity, natural hazards and land degradation) [17]–[19]. Synthetic aperture radar (SAR) [20] is the widely used sensor, which plays a very significant role in the remote sensing, earth observation and so on, and hence it is attracted in the military and civilian fields [20]–[25].

Bistatic SAR (BSAR) [26], compared with the monostatic SAR, has an advantage of the reduced vulnerability, which can allow the passive receiver to be located close to a hostile area but the vulnerable transmitter stays in a safe standoff

range [27]–[29]. And, BSAR has another advantage of the single-pass interferometry with a long baseline to greatly get the height accuracies [30]. Also, BSAR has the potential of the cost reduction by using one active transmitter and several passive receivers [31]. On account of the flexible deployment, BSAR can increase the scattered information; the reason is that the scattering characteristics of targets depend on the line-of-sight (LOS) vectors to receiver and transmitter [29].

P-band ultra-wideband (UWB [32]) BSAR system, in comparison with the P-band UWB monostatic SAR, is able to improve the foliage penetration ability due to the short integration time for the BSAR working in a long range [33], which can increase the detection performance of concealed targets under the foliage or subsurface. Besides, the P-band UWB BSAR has an increase of the target to clutter ratio, because the dihedral-like scattering mechanism dominates many of the strong clutter return [34]. Recently, the interest on the P-band UWB BSAR technique has rapidly increased, and then the UWB BSAR systems have been studied and built. So far, several UWB BSAR experiments with the different configurations have been carried out, and then the experimental results were also obtained [31]–[34].

However, P-band UWB BSAR raw data is of the huge amount, significant range-azimuth coupling, large spatial-variance, and complex motion error, which may increases the difficulty of the efficient and precise reconstruction of the raw data. In general, the BSAR raw data reconstruction strategy is classified into the time-domain reconstruction (TDR) and frequency-domain reconstruction (FDR), which can be developed and modified from the corresponding reconstruction strategy for the monostatic SAR raw data. Bistatic FDR strategy mainly includes the range Doppler (RD) method [35], frequency scaling (FS) method [36], Omega-k (WK) method [37], polar format (PF) method [38], chirp scaling (CS) method [39] and nonlinear CS (NCS) method [40]. However, the bistatic FDR strategy is only valid for the raw data reconstruction of some limited BSAR systems [35]–[40], because there is the approximate processing in the reconstruction of the BSAR raw data, including the approximation of the range-azimuth coupling, spatial-variance and motion error, which may cause some phase errors for the special bistatic case like the P-band UWB BSAR system. Luckily, the bistatic TDR strategy, like the backprojection (BP) method, is regarded as a linear transformation for the BSAR raw data processing, thus it can be used to reconstruct the BSAR image with the high-precision [41]. The bistatic BP method can work with almost all configurations of BSAR systems, thus there is no limitation for the speed, track, and altitude of the transmitter and receiver platforms, i.e., there is also no limit for the bistatic angle [46]. However, the bistatic BP method has a high computational complexity, which cannot be used as a standard strategy for BSAR data reconstruction.

In order to improve the reconstruction efficiency, the efficient realization of the bistatic BP method was studied, i.e., bistatic fast factorized BP (FFBP) method [42]–[49],

which was developed from the corresponding monostatic FFBP method [50]. Author of [42] first extended the FFBP method to reconstruction the one stationary BSAR raw data, but didn't provide the relational experiments. Author of [43] gave the basic principle of the bistatic FFBP method to focus the BSAR raw data, however, it didn't offer the specific realization. Author of [44] proposed a bistatic FFBP method for the spaceborne-airborne BSAR system, and it represented the subimage in the elliptical polar grid, which was only referenced to the track of the receiver or transmitter. However, in the derivation of the sampling requirement for the elliptical polar grid, only the linear track BSAR system with a higher angular velocity has been considered, therefore it was limited in some special BSAR circumstances. Based on [44], an improved bistatic FFBP method in the elliptical polar coordinate was proposed, it derived the sampling requirement for the elliptical polar grid considering the motion errors, while the elliptical polar grid was also only referenced to the transmitter track [45]. Authors of [46] presented a novel bistatic FFBP method based on the subapertures and local polar coordinates for the general airborne BSAR system, and the sampling requirements for the polar grids were derived in [47]. However, the motion error of the radar tracks was not considered in the derivation of the sampling requirement for the polar grids, which cannot offer a near-optimum trade-off between the phase errors and computational complexity. Authors of [46] also developed another bistatic FFBP method for the raw data reconstruction for the UWB BSAR system with a linear track, which was based on the subaperture processing and local beamforming [48]. However, it only provided the requirement for selecting the subapertures and subimages, but didn't offer the sampling requirements of the beams for corresponding subimages. Moreover, it requires the local beamforming from the radar raw data as an the intermediate processing in the ground plane, which cannot be exactly referenced to the radars' track considering the platform altitudes. Similarly, the motion error of the radar track was not considered in the derivation of the requirement or sampling requirement, which also cannot offer a near-optimum tradeoff between the phase error and computational complexity.

On the basis of the previous researches, we present a high-efficiency and high-precision reconstruction strategy for the P-band UWB BSAR raw data including the motion errors, which is also based on the subaperture processing and local beamforming [43], [48]. Compared with [48], in the presented method, the motion errors of the radar platforms are considered in the deviation of the requirement for selecting the subaperture and subimage and sampling requirement of the beam for the subimages, which can give a near-optimum tradeoff between the phase error and computational complexity in the P-band UWB BSAR raw data reconstruction. Besides, the presented method requires the local beamforming from the radar raw data as an intermediate processing step in the slant range plane instead of the ground plane, which can be accurately referenced to the tracks of the transmitter and receiver considering the platform altitudes.

Finally, the presented method not only can precisely handles the P-band UWB BSAR raw data of the huge amount, big spatial-variance, significant range-azimuth coupling and complicated motion error, but also keep the accuracy and robust of the FDR strategy but with a reduced computational complexity. A part of this work has been published in [49] and [51].

The organization of this paper is listed. In Section II, the geometric configuration of the P-band UWB BSAR is built, and the bistatic BP method for the raw data reconstruction is derived. In Section III, the subaperture processing and local beamforming in the presented FFBP method are proposed, and the requirement for selecting the subaperture and subimage is derived by analyzing the bistatic range error considering the motion errors, as well as the sampling requirement of the beam for subimages. The realization and computational complexity of the presented FFBP method are analyzed, and the speed-up factor of the presented FFBP method with respect to the bistatic BP method is derived. In Section IV, the presented FFBP method is tested and validated by the simulated and measured P-band UWB BSAR data. Section V provides a conclusion.

II. BISTATIC BP METHOD FOR P-BAND UWB BSAR
A. GEOMETRIC CONFIGURATION

Geometric configuration of the P-band UWB BSAR system with the platform altitude including the motion error can be shown in Fig.1. The ideal flight tracks of the transmitter and receiver are represented as the dashed beelines l_1 and l_3, but their actual tracks are represented as solid curves l_2 and l_4, respectively. $r_T(\eta) = (x_T(\eta), y_T(\eta), z_T(\eta))$ and $r_R(\eta) = (x_R(\eta), y_R(\eta), z_R(\eta))$ are the positions of the transmitter and the receiver at slow time η, respectively. Without loss of generality, in this geometric configuration, the receiver operates in the side-looking spotlight mode,

while the transmitter operates in the forward-looking spotlight mode [49]. Provided that the transmitter's illuminating beam is always covered by the receiver's illuminating beam to insure the synchronization of this P-band UWB BSAR system [49]. Suppose that P is an arbitrary scatterer in the illuminated scene, with the position $\mathbf{r}_P = (x_P, y_P, 0)$. Thus, the bistatic distance from the scatterer P to the transmitter and receiver at the slow time η is [49]

$$
\begin{aligned}
R(\eta, \mathbf{r}_P) &= R_T(\eta, \mathbf{r}_P) + R_R(\eta, \mathbf{r}_P) \\
&= \sqrt{(x_T(\eta) - x_P)^2 + (y_T(\eta) - y_P)^2 + (z_T(\eta))^2} \\
&\quad + \sqrt{(x_R(\eta) - x_P)^2 + (y_R(\eta) - y_P)^2 + (z_R(\eta))^2}.
\end{aligned}
\tag{1}
$$

Transmitted radar signal $p(\tau)$ is assumed to be the linear frequency modulation signal, after the range-compression, the received raw data from the scatterer P becomes [49]

$$
s_{rc}(\tau, \eta) = \sigma_P p_{rc} \left[B \left(\tau - \frac{R(\eta, \mathbf{r}_P)}{c} \right) \right] \exp \left[\frac{-j2\pi f_c R(\eta, \mathbf{r}_P)}{c} \right],
\tag{2}
$$

σ_P is the coefficient of the scatterer P, $p_{rc}[\cdot]$ is the range-compressed envelope, B is the bandwidth, τ is the fast time, c is the light speed, and f_c is the carried frequency.

B. BISTATIC BP METHOD

The backprojection of the range-compressed P-band UWB BSAR raw data in the bistatic BP method is performed over an ellipsoidal mapping [49]. Here, the foci of the mapped ellipsoid are the actual transmitter and receiver positions, which can be used to define the major axis of the mapped ellipsoid [48]. Provided that $\mathbf{r} = (x_m, y_n, 0)$ is an arbitrary sample in the illuminated scene, and the value of the P-band UWB BSAR image at the sample $\mathbf{r}$, reconstructed by the bistatic BP method [49], is given by

$$
I(\mathbf{r}) = \int_{\eta_c - T/2}^{\eta_c + T/2} s_{rc} \left(\frac{R(\eta, \mathbf{r})}{c}, \eta \right) \exp \left[\frac{j2\pi f_c R(\eta, \mathbf{r})}{c} \right] d\eta,
\tag{3}
$$

T is the integration time, and η_c is the time corresponding to the aperture center of the transmitter (receiver). $R(\eta, \mathbf{r})$ is the bistatic distance from the transmitter and receiver to the sample $\mathbf{r}$ at the slow time η [48], which is given by

$$
\begin{aligned}
R(\eta, \mathbf{r}) &= R_T(\eta, \mathbf{r}) + R_R(\eta, \mathbf{r}) \\
&= \sqrt{(x_T(\eta) - x_m)^2 + (y_T(\eta) - y_n)^2 + (z_T(\eta))^2} \\
&\quad + \sqrt{(x_R(\eta) - x_m)^2 + (y_R(\eta) - y_n)^2 + (z_R(\eta))^2}.
\end{aligned}
\tag{4}
$$

Note that, the sample $\mathbf{r}$ and other samples belonging to the reconstructed P-band UWB BSAR image, which have the same bistatic range $R(\eta, \mathbf{r})$, are assigned the same sample of the range-compressed raw data matched to this bistatic distance [48].
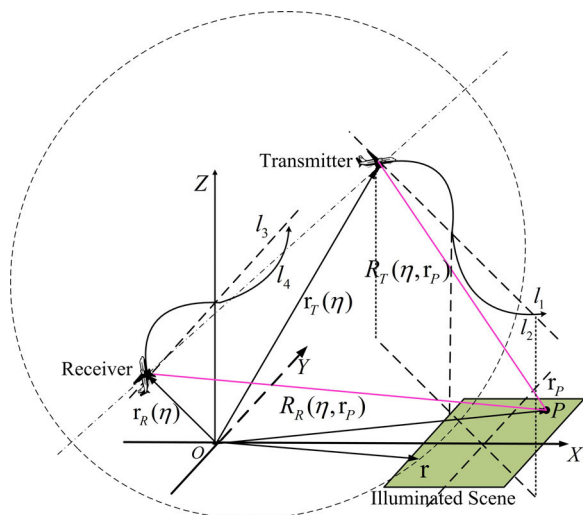

FIGURE 1. Geometric configuration of the P-band UWB BSAR system with the platform altitudes including the motion errors.

III. BISTATIC FFBP METHOD FOR P-BAND UWB BSAR

In this section, an improved bistatic FFBP method is proposed based on the subaperture processing and local beamforming, which is developed from the researches in [43] and [48], but the motion error is considered in the bistatic range error analysis to derive the requirement of selecting the subaperture and subimage, which can offer a near-optimum tradeoff between the precision and efficiency in the reconstruction of the P-band UWB BSAR raw data. Unlike the bistatic FFBP method given in [48], the local beamforming is highly performed in the slant range plane instead of the ground plane in the proposed FFBP method, which can be accurately referenced to the tracks of the transmitter and receiver considering the platform altitudes.
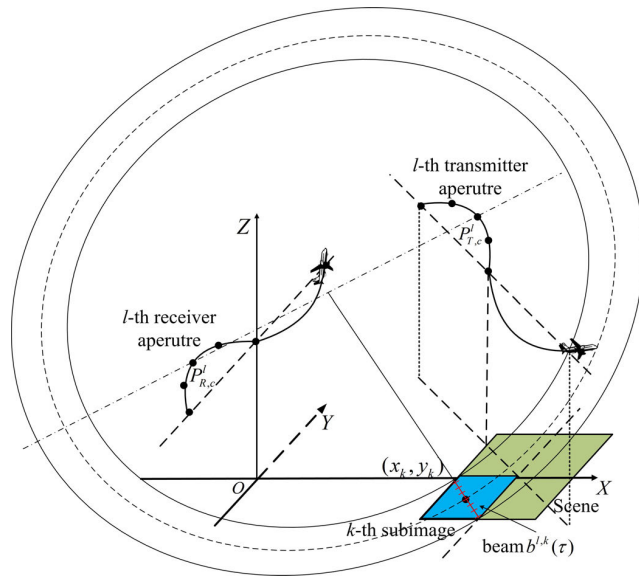

FIGURE 2. Subaperture processing and local beamforming in the proposed method.

A. SUBAPERTURE PROCESSING AND LOCAL BEAMFORMING

The subaperture processing and local beamforming in the proposed FFBP method is given in Fig.2. Provided that the complete transmitter and receiver apertures are split into L subapertures, while the full reconstructed P-band UWB BSAR scene is also split into K subimages. In Fig.2, $P_{T,c}^l$ and $P_{R,c}^l$ are defined as the centers of the l-th transmitter and receiver subaperture, respectively. (x_k, y_k) is defined as the center of the k-th subimage in the ground plane. For the l-th transmitter and receiver subapertures and the k-th subimage, the beam $b^{l,k}(\tau)$ is the link-line between center point of the positions $P_{T,c}^l$ and $P_{R,c}^l$ and the position (x_k, y_k). It is found that a minimum selection of the length of the beam $b^{l,k}(\tau)$ is limited by two solid ellipsoid [48]. The sample number of the beams should be selected to be big enough to cover the Nyquist sampling subimages [49], and therefore the sampling requirement of the beam $b^{l,k}(\tau)$ for the reconstruction of the P-band UWB BSAR raw data needs

to satisfy

$$\left| \Delta b^{l,k}(\tau) \right| \le c / B. \tag{5}$$

where, $R^l(\eta, x_k, y_k)$ is the bistatic distance from the aperture positions belonging to the l-th transmitter and receiver subapertures to the center of the k-th subimage, i.e., (x_k, y_k) at η [48], which is given by

$$\begin{aligned}
R^l(\eta, x_k, y_k) &= R_T^l(\eta, x_k, y_k) + R_R^l(\eta, x_k, y_k) \\
&= \sqrt{\left(x_T^l(\eta) - x_k\right)^2 + \left(y_T^l(\eta) - y_k\right)^2 + \left(z_T^l(\eta)\right)^2} \\
&\quad + \sqrt{\left(x_R^l(\eta) - x_k\right)^2 + \left(y_R^l(\eta) - y_k\right)^2 + \left(z_R^l(\eta)\right)^2}. \tag{6}
\end{aligned}$$

where, $(x_T^l(\eta), y_T^l(\eta), z_T^l(\eta))$ and $(x_R^l(\eta), y_R^l(\eta), z_R^l(\eta))$ indicate the aperture positions belonging to the l-th transmitter and receiver subapertures at the slow time η, respectively. In the local beamforming, all the range-compressed raw data $s_{rc}(\tau, \eta)$ belonging to the l-th transmitter and receiver subapertures are shifted in the fast time $R^l(\eta, x_k, y_k)/c$, so the shifted range-compressed raw data in the fast time τ is represented as $s_{rc}(\tau + R^l(\eta, x_k, y_k)/c, \eta)$ [49]. And, the shifted range-compressed raw data belonging to the l-th transmitter and receiver subapertures are projected into the samples of the beam $b^{l,k}(\tau)$ over an elliptical mapping in Fig.2, and then added coherently to form the beam $b^{l,k}(\tau)$, which is

$$\begin{aligned}
b^{l,k}(\tau) = \int_{\eta_c^l - T^l/2}^{\eta_c^l + T^l/2} s_{rc}\left(\tau + \frac{R^l(\eta, x_k, y_k)}{c}, \eta\right) \\
\times \exp\left[j2\pi f_c\left(\tau + \frac{R^l(\eta, x_k, y_k)}{c}\right)\right] d\eta, \tag{7}
\end{aligned}$$

η_c^l is the slow time corresponding to the l-th subaperture center, and T^l is the integration time of the l-th subaperture.

B. REQUIREMENT FOR SELECTING SUBAPERTURE AND SUBIMAGE BY ANALYZING BISTATIC RANGE ERROR COSIDERING MOTION ERRORS

For the l-th transmitter and receiver subapertures, the bistatic range error analysis considering the motion errors is shown in Fig.3. Let us consider one of the aperture positions belonging to the l-th transmitter subaperture (e.g. the first one), the sample (x_m, y_n) belonging to the k-th subimage, the corresponding aperture position belonging to the l-th receiver subaperture (e.g. also the first one) [49]. The true bistatic distance from the considered transmitter and receiver aperture positions to sample (x_m, y_n) is marked by the black dashed lines in Fig.3, which is given by

$$R^{l,k,m,n} = R_T^{l,k,m,n} + R_R^{l,k,m,n}, \tag{8}$$

$R_R^{l,k,m,n}$ is the distance from the considered receiver aperture position to the sample (x_m, y_n), but $R_T^{l,k,m,n}$ is the distance from the considered transmitter aperture position to the sample (x_m, y_n). In the proposed FFBP method, the sample
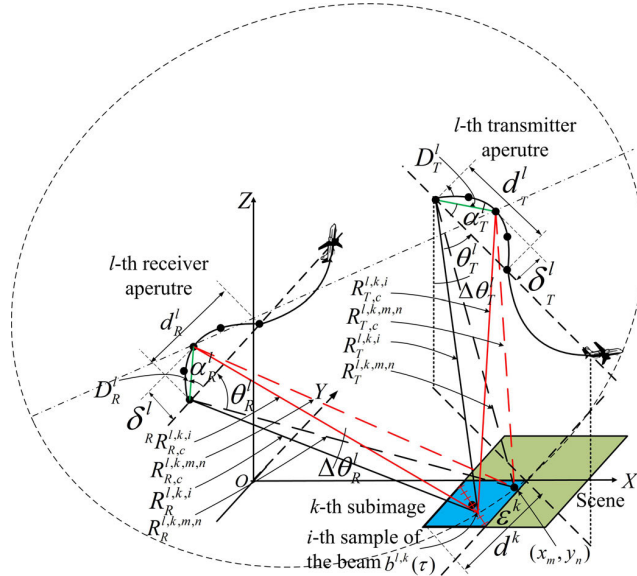
FIGURE 3. Bistatic range error analysis considering the motion errors.

(x_m, y_n) belonging to the k-th subimage is actually mapped by the i-th sample of the beam $b^{l,k}(\tau)$ over an elliptical mapping, and this mapping is marked by a dashed ellipsoid in Fig.3, whose major axis is the link-line between the center of the l-th transmitter and receiver subapertures [48]. Hence, the processed bistatic distance is the range from the considered transmitter and receiver aperture positions to the i-th sample of the beam $b^{l,k}(\tau)$, which can be marked by the black solid lines in Fig.3, which is given by

$$R^{l,k,i} = R_T^{l,k,i} + R_R^{l,k,i}, \tag{9}$$

$R_R^{l,k,i}$ is the distance from the considered receiver aperture position to the i-th sample of the beam $b^{l,k}(\tau)$, but $R_T^{l,k,i}$ is the distance between the considered transmitter aperture position and the i-th sample of the beam $b^{l,k}(\tau)$. There is a difference between the true bistatic distance $R^{l,k,m,n}$ and processed bistatic distance $R^{l,k,i}$, which may causes phase errors in the P-band UWB BSAR raw data reconstruction.

The bistatic distance from the centers of the l-th transmitter and receiver subapertures to the sample (x_m, y_n) is marked by a red dashed lines in Fig.3, which is given by

$$R_c^{l,k,m,n} = R_{T,c}^{l,k,m,n} + R_{R,c}^{l,k,m,n}, \tag{10}$$

where, $R_{R,c}^{l,k,m,n}$ is the distance from the center of the l-th receiver subaperture to the sample (x_m, y_n), while $R_{T,c}^{l,k,m,n}$ is the distance between the center of the l-th transmitter subaperture and the sample (x_m, y_n). The bistatic distance from the center of the l-th transmitter and receiver subapertures to the i-th sample of the beam $b^{l,k}(\tau)$ can be marked by the red solid lines in Fig.3, which is given by

$$R_c^{l,k,i} = R_{T,c}^{l,k,i} + R_{R,c}^{l,k,i}, \tag{11}$$

$R_{R,c}^{l,k,i}$ is the distance from the center of the l-th receiver subaperture to the i-th sample of the beam $b^{l,k}(\tau)$, while

$R_{T,c}^{l,k,i}$ is the range between the center of the l-th transmitter subaperture and the i-th sample of the beam $b^{l,k}(\tau)$.

Let d_R^l be the length of the l-th receiver subaperture along the receiver ideal track, but δ_R^l is the across-track deviation of the l-th receiver subaperture along the LOS direction from the receiver ideal track [49]. Analogously, d_T^l can be used to denote the length of the l-th transmitter subaperture along the transmitter ideal track, and δ_T^l is used to denote the across-track deviation of the l-th transmitter subaperture along the LOS direction from the transmitter ideal track. As show in [49], D_R^l is the beeline between the l-th receiver subaperture center and the considered receiver aperture position, with its length $D_R^l = \sqrt{\left(d_R^l/2\right)^2 + \left(\delta_R^l\right)^2}$. D_T^l is the beeline between the l-th transmitter subaperture center and considered transmitter aperture position, and its length is $D_T^l = \sqrt{\left(d_T^l/2\right)^2 + \left(\delta_T^l\right)^2}$. The angle from the beeline D_R^l to the receiver ideal flight is α_R^l, but α_T^l indicates the angle from the beeline D_T^l to the transmitter ideal flight. The angle from the distance $R_R^{l,k,m,n}$ to the receiver ideal flight is θ_R^l, but θ_T^l is the angle from the distance $R_T^{l,k,m,n}$ to the transmitter ideal flight. Let $\Delta\theta_R^l$ be the angle between the distances $R_R^{l,k,m,n}$ and $R_R^{l,k,i}$, and the angle between the distances $R_T^{l,k,m,n}$ and $R_T^{l,k,i}$ is $\Delta\theta_T^l$. ε^k is defined as the space between the sample (x_m, y_n) and the i-th sample of the beam $b^{l,k}(\tau)$ belonging to the k-th subimage ellipsoidaly mapped by that beam sample. Since the maximum value of ε^k is not more than half of the maximum dimension of the k-th subimage, i.e., the diagonal of the k-th subimage d^k, thus $\varepsilon^k \leq d^k/2$ is reasonable in reality [48]. Applying the law of cosine, the monostatic distance $R_T^{l,k,i}$ is calculated and expanded using the Taylor series [49], which is

$$R_T^{l,k,i}$$
$$= \left[\left(R_{T,c}^{l,k,i}\right)^2 + \left(D_T^l\right)^2 - 2R_{T,c}^{l,k,i}D_T^l\cos\left(\theta_T^l + \Delta\theta_T^l + \alpha_T^l\right)\right]^{1/2}$$
$$= R_{T,c}^{l,k,i} - D_T^l\cos\left(\theta_T^l + \Delta\theta_T^l + \alpha_T^l\right)$$
$$+ \left(D_T^l\right)^2\sin^2\left(\theta_T^l + \Delta\theta_T^l + \alpha_T^l\right)\Big/2R_{T,c}^{l,k,i} + \cdots \tag{12}$$

Due to $D_T^l \ll R_{T,c}^{l,k,i}$, the distance $R_T^{l,k,i}$ is approximated as

$$R_T^{l,k,i} \approx R_{T,c}^{l,k,i} - D_T^l\cos\left(\theta_T^l + \Delta\theta_T^l + \alpha_T^l\right). \tag{13}$$

Similarly, $R_R^{l,k,i}$ can be calculated and approximated as

$$R_R^{l,k,i}$$
$$= \left[\left(R_{R,c}^{l,k,i}\right)^2 + \left(D_R^l\right)^2 - 2R_{R,c}^{l,k,i}D_R^l\cos\left(\theta_R^l + \Delta\theta_R^l + \alpha_R^l\right)\right]^{1/2}$$
$$\approx R_{R,c}^{l,k,i} - D_R^l\cos\left(\theta_R^l + \Delta\theta_R^l + \alpha_R^l\right) \tag{14}$$

Analogously, the monostatic distances $R_T^{l,k,m,n}$ and $R_R^{l,k,m,n}$ can be respectively calculated and then approximated as

$$\begin{cases} R_T^{l,k,m,n} \approx R_{T,c}^{l,k,m,n} - D_T^l\cos\left(\theta_T^l + \alpha_T^l\right) \\ R_R^{l,k,m,n} \approx R_{R,c}^{l,k,m,n} - D_R^l\cos\left(\theta_R^l + \alpha_R^l\right). \end{cases} \tag{15}$$

On the basis of the property of the ellipse in Fig.3, we have

$$R_{T,c}^{l,k,m,n} + R_{R,c}^{l,k,m,n} = R_{T,c}^{l,k,i} + R_{R,c}^{l,k,i}. \qquad (16)$$

The bistatic distance error between the sample (x_m, y_n) belonging to the k-th subimage and the i-th sample of the beam $b^{l,k}(\tau)$ is given by

$$
\begin{aligned}
\Delta R^{l,k} &= R^{l,k,m,n} - R^{l,k,i} \\
&\approx D_T^l \left[\cos\left(\theta_T^l + \Delta\theta_T^l + \alpha_T^l\right) - \cos\left(\theta_T^l + \alpha_T^l\right) \right] \\
&\quad + D_R^l \left[\cos\left(\theta_R^l + \Delta\theta_R^l + \alpha_R^l\right) - \cos\left(\theta_R^l + \alpha_R^l\right) \right].
\end{aligned} \qquad (17)
$$

Since the value of the angles $\Delta\theta_T^l$ and $\Delta\theta_R^l$ is usually very small for the l-th transmitter and receiver subapertures, then the bistatic range error $\Delta R^{l,k}$ is further approximated as [49]

$$\Delta R^{l,k} \approx -D_T^l \sin(\theta_T^l + \alpha_T^l)\Delta\theta_T^l - D_R^l \sin(\theta_R^l + \alpha_R^l)\Delta\theta_R^l. \qquad (18)$$

According to the geometric configuration in Fig.3, we have

$$
\begin{cases}
\left|\sin(\theta_T^l + \alpha_T^l)\right| \le 1, & \left|\sin(\theta_R^l + \alpha_R^l)\right| \le 1 \\
\left|\Delta\theta_T^l\right| \approx \dfrac{\varepsilon^k}{R_{T,c}^{l,k,m,n}} \le \dfrac{d^k}{2R_{T,c,\min}^{l,k,m,n}}, & \left|\Delta\theta_R^l\right| \approx \dfrac{\varepsilon^k}{R_{R,c}^{l,k,m,n}} \le \dfrac{d^k}{2R_{R,c,\min}^{l,k,m,n}}
\end{cases} \qquad (19)
$$

where, $R_{T,c,\min}^{l,k,m,n}$ and $R_{R,c,\min}^{l,k,m,n}$ are the minimum value of these monostatic distances $R_{T,c}^{l,k,m,n}$ and $R_{R,c}^{l,k,m,n}$, respectively. Using the definition in [49], the upper bound of the bistatic range error is given by

$$
\begin{aligned}
&\left|\Delta R^{l,k}\right| \\
&\le \frac{D_T^l d^l}{2R_{T,c,\min}^{l,k,m,n}} + \frac{D_R^l d^l}{2R_{R,c,\min}^{l,k,m,n}} \\
&= \frac{d^k}{4} \left[\frac{\sqrt{\left(d_T^l\right)^2 + \left(2\delta_{T,\max}^l\right)^2}}{R_{T,c,\min}^{l,k,m,n}} + \frac{\sqrt{\left(d_R^l\right)^2 + \left(2\delta_{R,\max}^l\right)^2}}{R_{R,c,\min}^{l,k,m,n}} \right].
\end{aligned} \qquad (20)
$$

$\delta_{T,\max}^l$ and $\delta_{R,\max}^l$ are the maximum value of the distances δ_T^l and δ_R^l. Thus, the maximum phase error caused by the bistatic range error is given by

$$
\begin{aligned}
&\Delta\phi_{\max}^{l,k} \\
&= \frac{\pi d^k}{2\lambda_{\min}} \left[\frac{\sqrt{\left(d_T^l\right)^2 + \left(2\delta_{T,\max}^l\right)^2}}{R_{T,c,\min}^{l,k,m,n}} + \frac{\sqrt{\left(d_R^l\right)^2 + \left(2\delta_{R,\max}^l\right)^2}}{R_{R,c,\min}^{l,k,m,n}} \right].
\end{aligned} \qquad (21)
$$

where $\lambda_{\min}$ is the minimum radar wavelength.

On the basis of [50], if the maximum phase error of the FFBP method is smaller than or equal to $\pi/8$, the phase error effect caused by the range error can be neglected in the reconstruction of the SAR raw data with the far-field configuration. Therefore, the requirement of selecting the subaperture and subimage for the l-th transmitter and receiver subapertures can be given by (22), shown at the bottom of this page.

C. REALIZATION PROCEDURE

The realization procedure of the proposed FFBP method for reconstructing the P-band UWB BSAR raw data is similar to that of the bistatic FFBP method given in [48], while it calculates the subimages on the beams in the slant range plane instead of the ground plane, which can be accurately referenced to positions of the transmitter and receiver. Analogously, the reconstruction of the P-band UWB BSAR raw data by the proposed FFBP method can be divided into two steps: beamforming (BF) step and backprojection (BP) step [49]. The realization procedure of the proposed FFBP method is shown in Fig.4. The BF step is included in the red dashed rectangle, while the BP step is included in the purple dashed rectangle.

Provided that the number of the aperture positions for both transmitter and receiver are N_L. Further assumed that it can be found a factorization of the number of the aperture positions N_L into P integer factors matching to P steps [49], which is given by

$$N_L = \prod_{p=1}^{P} F_p \quad p = 1, \cdots, P, \qquad (23)$$

where F_p is the reduction in the number N_L for the transmitter and receiver during the p-th step.

In the first BF step, the full transmitter and receiver apertures are firstly split into L_1 first order subapertures. In addition, the complete reconstructed P-band UWB BSAR scene is split into K_1 first order subimage according to (22). Then, the first order beams are defined as the link-line between the center point of the l_1-th transmitter and receiver subaperture centers and the center of the k_1-th subimage, and these beams are sampled according to the sampling requirement in (5). At last, the range-compressed raw data belonging to l_1-th transmitter and receiver subaperture are shifted with respect to the center of the k_1-th subimage, and the shifted range-compressed raw data are projected into the beam samples of the first order beam $b^{l_1,k_1}(\tau)$ over an ellipsoid, finally accumulated coherently to form the first order beam $b^{l_1,k_1}(\tau)$ [48], which is given

$$d^k \le \frac{\lambda_{\min} R_{T,c,\min}^{l,k,m,n} R_{R,c,\min}^{l,k,m,n}}{4\left[R_{R,c,\min}^{l,k,m,n} \sqrt{\left(d_T^l\right)^2 + \left(2\delta_{T,\max}^l\right)^2} + R_{T,c,\min}^{l,k,m,n} \sqrt{\left(d_R^l\right)^2 + \left(2\delta_{R,\max}^l\right)^2} \right]} \qquad (22)$$
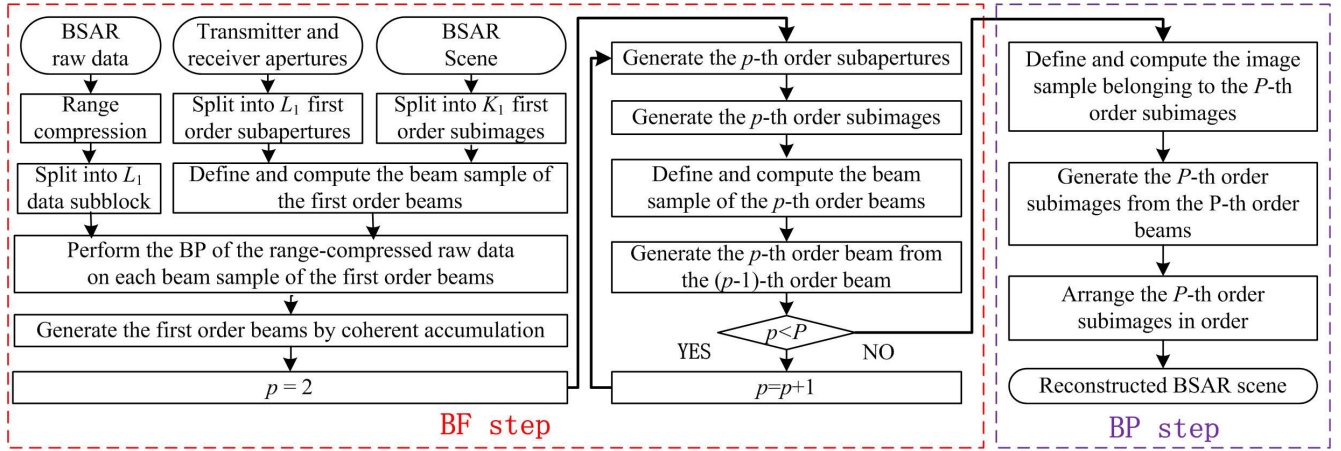
FIGURE 4. Realization procedure of the proposed FFBP method for reconstructing the P-band UWB BSAR raw data.

by

$$
b^{l_1,k_1}(\tau) = \int_{\eta_c^{l_1}-T^{l_1}/2}^{\eta_c^{l_1}+T^{l_1}/2} s_{rc}\left(\tau + \frac{R^{l_1}(\eta, x_{k_1}, y_{k_1})}{c}, \eta\right)
$$
$$
\cdot \exp\left[j2\pi f_c\left(\tau + \frac{R^{l_1}(\eta, x_{k_1}, y_{k_1})}{c}\right)\right]d\eta, \quad (24)
$$

where, $\eta_c^{l_1}$ is the slow time corresponding the l_1-th subaperture center and T^{l_1} is the integration time for the l_1-th subaperture. $R^l(\eta, x_k, y_k)$ is the bistatic distance from the aperture positions belonging to the l_1-th transmitter and receiver subaperture to the center position of the k_1-th subimage, i.e., (x_{k_1}, y_{k_1}) at the slow time η, which is

$$
R^{l_1}(\eta, x_{k_1}, y_{k_1})
$$
$$
= R_T^{l_1}(\eta, x_{k_1}, y_{k_1}) + R_R^{l_1}(\eta, x_{k_1}, y_{k_1})
$$
$$
= \sqrt{\left(x_T^{l_1}(\eta) - x_{k_1}\right)^2 + \left(y_T^{l_1}(\eta) - y_{k_1}\right)^2 + \left(z_T^{l_1}(\eta)\right)^2}
$$
$$
+ \sqrt{\left(x_R^{l_1}(\eta) - x_{k_1}\right)^2 + \left(y_R^{l_1}(\eta) - y_{k_1}\right)^2 + \left(z_R^{l_1}(\eta)\right)^2}. \quad (25)
$$

$\left(x_T^{l_1}(\eta), y_T^{l_1}(\eta), z_T^{l_1}(\eta)\right)$ and $\left(x_R^{l_1}(\eta), y_R^{l_1}(\eta), z_R^{l_1}(\eta)\right)$ are respectively the aperture positions belonging to the l_1-th transmitter and receiver subapertures at the slow time η. After the first BF step, $L_1 \times K_1$ first order beams are formed to cover K_1 subimages [49]. The sample number of the beams should be selected big enough to cover the beams created in the next BF step [48].

In the p-th ($1 < p < P$) BF step, the p-th order beams can be generated from the $(p-1)$-th order beams formed in the last BF step [49]. At the beginning, every F_p smaller $(p-1)$-th order transmitter subapertures in order are combined together to form a larger p-th order subaperture, therefore the number of the transmitter subapetures is reduced from L_{p-1} to L_p. This step is used to the same number of $(p-1)$-th order receiver subaperture, and the number of the receiver subapetures is reduced to from L_{p-1} to L_p. Conversely, the larger

$(p-1)$-th order subimages are further split into a number of the smaller p-th order subimages, thus the number of the subimages increases from K_{p-1} to K_p. Second, the p-th order beams are defined as the link-line between the center point of the l_p-th transmitter and receiver subaperture centers and the center of the k_p-th subimage. Finally, each beam sample of the p-th order beam $b^{l_p,k_p}(\tau)$ is projected from the beam samples of the $(p-1)$-th order beam $b^{l_{p-1},k_{p-1}}(\tau)$ over an ellipsoid, and supposed coherently to form the p-th order beam $b^{l_p,k_p}(\tau)$ [48], which is

$$
b^{l_p,k_p}(\tau) = \sum_{l_{p-1}=1+(l_p-1)F_p}^{l_pF_p} b^{l_{p-1},k_{p-1}}\left[\tau + \frac{\Delta R}{c}\right]
$$
$$
\times \exp\left[j2\pi f_c\left(\frac{\Delta R}{c}\right)\right], \quad (26)
$$

where ΔR is the bistatic distance difference, which is

$$
\Delta R = R_c^{l_{p-1}}(x_{k_p}, y_{k_p}) - R_c^{l_{p-1}}(x_{k_{p-1}}, y_{k_{p-1}}). \quad (27)
$$

where

$$
R_c^{l_{p-1}}(x_{k_p}, y_{k_p})
$$
$$
= R_{T,c}^{l_{p-1}}(x_{k_p}, y_{k_p}) + R_{R,c}^{l_{p-1}}(x_{k_p}, y_{k_p})
$$
$$
= \sqrt{\left(x_{T,c}^{l_{p-1}} - x_{k_p}\right)^2 + \left(y_{T,c}^{l_{p-1}} - y_{k_p}\right)^2 + \left(z_{T,c}^{l_{p-1}}\right)^2}
$$
$$
+ \sqrt{\left(x_{R,c}^{l_{p-1}} - x_{k_p}\right)^2 + \left(y_{R,c}^{l_{p-1}} - y_{k_p}\right)^2 + \left(z_{R,c}^{l_{p-1}}\right)^2}. \quad (28)
$$

and

$$
R_c^{l_{p-1}}(x_{k_{p-1}}, y_{k_{p-1}})
$$
$$
= R_{T,c}^{l_{p-1}}(x_{k_{p-1}}, y_{k_{p-1}}) + R_{R,c}^{l_{p-1}}(x_{k_{p-1}}, y_{k_{p-1}})
$$
$$
= \sqrt{\left(x_{T,c}^{l_{p-1}} - x_{k_{p-1}}\right)^2 + \left(y_{T,c}^{l_{p-1}} - y_{k_{p-1}}\right)^2 + \left(z_{T,c}^{l_{p-1}}\right)^2}
$$
$$
+ \sqrt{\left(x_{R,c}^{l_{p-1}} - x_{k_{p-1}}\right)^2 + \left(y_{R,c}^{l_{p-1}} - y_{k_{p-1}}\right)^2 + \left(z_{R,c}^{l_{p-1}}\right)^2}. \quad (29)
$$

where, $\left(x_{T,c}^{l_{p-1}}, y_{T,c}^{l_{p-1}}, z_{T,c}^{l_{p-1}}\right)$ and $\left(x_{R,c}^{l_{p-1}}, y_{R,c}^{l_{p-1}}, z_{R,c}^{l_{p-1}}\right)$ indicate the centers of the l_{p-1}-th transmitter and receiver subapertures, respectively. $(x_{k_{p-1}}, y_{k_{p-1}})$ and (x_{k_p}, y_{k_p}) are the centers of the k_{p-1}-th subimage and k_p-th subimage, respectively. After the p-th BF step, $L_p \times K_p$ p-th order beams are formed to cover K_p subimages [49]. It is found that this step is repeated until the final BF step. Please note that the sample number of the beams should be selected big enough to cover either the beams created in next BF step if there are any or the subimages in the BP step [48].

In the BP step (i.e., the P-th step), in order to reduce the computational complexity, the $(P\text{-}1)$-th order beams are used to form K_P the P-th order subimages in the ground plane over an ellipsoid [49]. Firstly, all F_p smaller $(P\text{-}1)$-th order transmitter subapertures are combined together to generate the complete transmitter aperture. This step is applied to the same number of $(P\text{-}1)$-th order receiver subapertures. While, the larger $(P\text{-}1)$-th order subimages are further split into a number of smaller P-th order subimages, thus number of the subimages increases from K_{P-1} to K_P. Secondly, the image grid (x_m, y_n) belonging to the k_p-th P-th order subimage in the ground plane is defined, i.e., (x_{m,k_P}, y_{n,k_P}). Finally, the beam samples of the k_{p-1}-th $(P\text{-}1)$-th order beams are projected into the image grid (x_{m,k_P}, y_{n,k_P}) and added coherently to form the k_p-th P-th order subimage, which is given by

$$I^{k_P}(x_{m,k_P}, y_{n,k_P})$$
$$= \sum_{l_{P-1}=1}^{F_P} b^{l_{P-1},k_{P-1}} \left[\frac{R_c^{l_{P-1}}(x_{m,k_P}, y_{n,k_P}) - R_c^{l_{P-1}}(x_{k_{P-1}}, y_{k_{P-1}})}{c} \right]$$
$$\cdot \exp\left[j2\pi f_c \left(\frac{R_c^{l_{P-1}}(x_{m,k_P}, y_{n,k_P}) - R_c^{l_{P-1}}(x_{k_{P-1}}, y_{k_{P-1}})}{c} \right) \right] \tag{30}$$

where

$$R_c^{l_{P-1}}(x_{m,k_P}, y_{n,k_P})$$
$$= R_{T,c}^{l_{P-1}}(x_{m,k_P}, y_{n,k_P}) + R_{R,c}^{l_{P-1}}(x_{m,k_P}, y_{n,k_P})$$
$$= \sqrt{\left(x_{T,c}^{l_{P-1}} - x_{m,k_P}\right)^2 + \left(y_{T,c}^{l_{P-1}} - y_{n,k_P}\right)^2 + \left(z_{T,c}^{l_{P-1}}\right)^2}$$
$$+ \sqrt{\left(x_{R,c}^{l_{P-1}} - x_{m,k_P}\right)^2 + \left(y_{R,c}^{l_{P-1}} - y_{n,k_P}\right)^2 + \left(z_{R,c}^{l_{P-1}}\right)^2} \tag{31}$$

and

$$R_c^{l_{P-1}}(x_{k_{P-1}}, y_{k_{P-1}})$$
$$= R_{T,c}^{l_{P-1}}(x_{k_{P-1}}, y_{k_{P-1}}) + R_{R,c}^{l_{P-1}}(x_{k_{P-1}}, y_{k_{P-1}})$$
$$= \sqrt{\left(x_{T,c}^{l_{P-1}} - x_{k_{P-1}}\right)^2 + \left(y_{T,c}^{l_{P-1}} - y_{k_{P-1}}\right)^2 + \left(z_{T,c}^{l_{P-1}}\right)^2}$$
$$+ \sqrt{\left(x_{R,c}^{l_{P-1}} - x_{k_{P-1}}\right)^2 + \left(y_{R,c}^{l_{P-1}} - y_{k_{P-1}}\right)^2 + \left(z_{R,c}^{l_{P-1}}\right)^2} \tag{32}$$

where, $\left(x_{T,c}^{l_{P-1}}, y_{T,c}^{l_{P-1}}, z_{T,c}^{l_{P-1}}\right)$ and $\left(x_{R,c}^{l_{P-1}}, y_{R,c}^{l_{P-1}}, z_{R,c}^{l_{P-1}}\right)$ indicate the centers of the l_{P-1}-th transmitter and receiver

subapertures, respectively. $(x_{k_{P-1}}, y_{k_{P-1}})$ is the center of the k_{P-1}-th subimage.

The final P-band UWB BSAR image is obtained by a union of all subimages in a correct order, which depends on how the P-band UWB BSAR scene is split at the outset [48]. Firstly, K_P P-th order subimages can be arranged to build up K_{P-1} $(P\text{-}1)$-th order subimages, until K_1 first-order subimages are obtained. Secondly, these K_1 first-order subimages are combined to reconstruct the complete P-band UWB BSAR scene. Therefore, the final expression of the proposed FFBP method is given by

$$I(x_m, y_n)$$
$$= \bigcup_{k_1=1}^{K_1} \bigcup_{k_2=1+(k_1-1)(K_2/K_1)}^{k_1(K_2/K_1)} \cdots \bigcup_{k_p=1+(k_{p-1}-1)(K_p/K_{p-1})}^{k_{p-1}(K_p/K_{p-1})}$$
$$\cdots \bigcup_{k_P=1+(k_P-1)(K_P/K_{P-1})}^{k_P(K_P/K_{P-1})} I^{k_P}(x_{m,k_P}, y_{n,k_P}) \tag{33}$$

D. COMPUTATIONAL COMPLEXITY

The computational complexity (operation number) of the proposed FFBP method mainly includes the operation numbers of the BF and BP, which not only depends on the number of the transmitter and receiver aperture positions and sample number of the P-band UWB BSAR scene, but also is dependent on the selection of the subaperture length and subimage area size [45].

For simplification, it is assumed that there is a constant factorization of the number of transmitter and receiver aperture positions N_L during all steps, i.e., $N_L = F^P$ ($F_p \equiv F$ for all p). According to the theoretic resolutions of the Cartesian BSAR image, we can define that the BSAR scene has samples $N_A \times N_R$ in the azimuth and range, respectively. For the first BF step, provided that the number of the beam sample of all first order beam is N_{B1}, thus the number of the operation to form the first order beams at this step is given by

$$O_1 = (N_{B1} \cdot F) \cdot L_1 \cdot K_1 = N_{B1}K_1N_L, \tag{34}$$

where $F \cdot L_1 = N_L$. For the p-th ($1 < p < P - 1$) BF step, provided that the number of the beam sample of all p-th order beam is N_{Bp}. It can be assumed that $N_{Bp} \approx N_{B1}/F^{p-1}$, thus the number of the operation to form the p-th order beams at the p-th BF step can be calculated in a similar way, which is

$$O_p = (N_{Bp} \cdot F) \cdot L_p \cdot K_p$$
$$= \left[\frac{N_{B1}}{F^{p-1}} \cdot F \right] \cdot \frac{L_1}{F^{p-1}} \cdot \left[K_1 \cdot F^{2(p-1)} \right] = N_{B1}K_1N_L. \tag{35}$$

Hence, the total number of the operation to form all beams at the BF step is computed by

$$O_{BF} = \sum_{p=1}^{P-1} O_p = (P-1)N_{B1}K_1N_L. \tag{36}$$

For the BP step, the number of the operation to reconstruct the P-band UWB BSAR scene in the ground plane is

given by

$$O_{BP} = N_{SI} \cdot L_{P-1} \cdot K_P$$
$$= \left[\frac{N_A \cdot N_R}{K_1 \cdot F^{2(P-1)}} \right] \cdot \frac{L_1}{F^{P-2}} \cdot \left[K_1 \cdot F^{2(P-1)} \right] = N_A N_R F,$$
(37)

where, N_{SI} is the number of each subimage samples at the BP step. Hence, the total operation number (computational complexity) of the proposed FFBP method is given by

$$O_{\text{FFBP Method}} = O_{BF} + O_{BP} = (P-1)N_{B1}K_1 N_L + N_A N_R F$$
(38)

In the P-band UWB BSAR scene reconstruction, the number of the aperture positions of the transmitter and receiver subapertures (i.e., the length of the transmitter and receiver subapertures) are usually inversely proportional to the number of the subimage samples (i.e., the square root of the square subimage area) [48]. For the first BF step, there is relationship

$$F = N_L / L_1 = \mu \sqrt{K_1 / (N_A \cdot N_R)}.$$
(39)

where μ is an integer number ($\mu \gg 1$). Because the maximum value of the beam samples N_{B1} is not more than the maximum dimension of the first order subimage, we can assume that

$$N_{B1} \approx \sqrt{\left(\frac{N_A}{\sqrt{K_1}}\right)^2 + \left(\frac{N_R}{\sqrt{K_1}}\right)^2} = \sqrt{\frac{N_A^2 + N_R^2}{K_1}}.$$
(40)

Substituting (39) and (40) into (38), the operation number (computational complexity) of the proposed FFBP method is given by

$$O_{\text{FFBP Method}}$$
$$= \frac{(P-1)N_L F}{\mu} \sqrt{\left(N_A^2 + N_R^2\right) N_A N_R} + N_A N_R F$$
$$= \frac{(\log_F N_L - 1)N_L F}{\mu} \sqrt{\left(N_A^2 + N_R^2\right) N_A N_R} + N_A N_R F.$$
(41)

Similarly, the computational complexity to reconstruct the P-band UWB BSAR scene by the bistatic BP method can be also computed as [45]

$$O_{\text{BP Method}} = (N_A \cdot N_R) N_L.$$
(42)

According to [45], the speed-up factor of the proposed FFBP method with respect to the bistatic BP method is defined as (43), shown at the bottom of this page.

It is found that the speed-up factor κ is determined by the factors N_A, N_R, N_L, F and μ. When the number of the transmitter and receiver aperture position N_L increases, only

the factor $\log_F N_L$ in (43) increases, where N_A, N_R, F and μ are assumed to be constant. Taking an example to examine the computational complexity of the proposed FFBP method with respect to the bistatic BP method. We assume that the BSAR scene is square, i.e., $N_A = N_R = N$, and then the number of the transmitter and receiver aperture positions is assumed to be N, i.e., $N_L = N$, and the integer number μ is also assumed to be N, i.e., $\mu = N$. The speed-up factor κ is simplify given by

$$\kappa = N \Big/ F \left[\sqrt{2}(\log_F N - 1) + 1 \right].$$
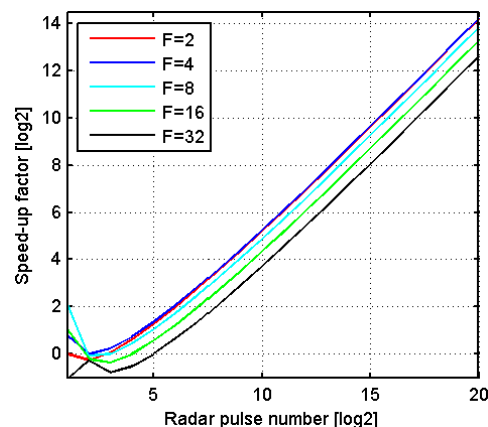(44)

FIGURE 5. Logarithm (base 2) of the speed-up factor of the proposed FFBP method.

From (44), it can be found that the computational complexity of the proposed FFBP method is reduced approximately κ times compared with the bistatic BP method. According to (44), the logarithm (base 2) of the speed-up factor κ with respect to N for the different factorization F is shown in Fig.5. In Fig.5, it is seen that the logarithm of the speed-up factors marked by the different colors are almost directly proportional to $\log_2 N$ in the most range. It can be found that, the larger the factorization F, the smaller the speed-up factor κ. Moreover, for a constant value of F, as the radar pulse number N increases, the speed-up factor κ increases. In addition, the speed-up factor κ for different factorization F are smaller than one, when the radar pulse number N is very small. It can be found that the reason is that the proposed FFBP method has more operation number on the calculation and interpolation of the beam samples than that of the bistatic BP method [45]. In comparison to the bistatic BP method, the proposed FFBP method has a well acceleration for the high resolution reconstruction of the P-band UWB BSAR raw data, but doesn't offer any acceleration for the low-moderate resolution reconstruction of the P-band UWB BSAR raw data [45].

$$\kappa = \frac{O_{\text{BP Method}}}{O_{\text{FFBP Method}}} \frac{\mu N_A N_R N_L}{\left[(\log_F N_L - 1)N_L F \right] \sqrt{\left(N_A^2 + N_R^2\right) N_A N_R + \mu N_A N_R F}}.$$
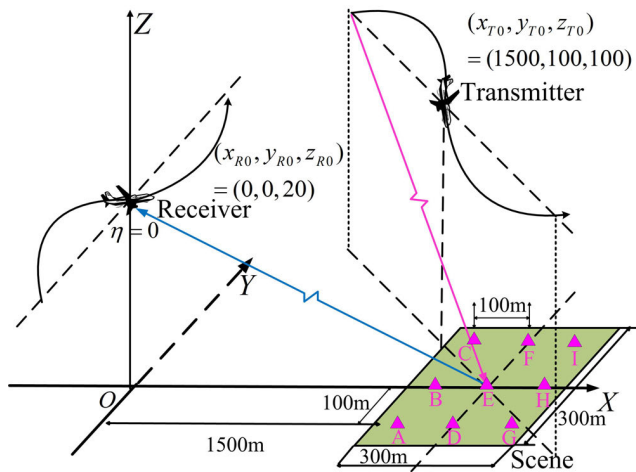(43)

FIGURE 6. Geometric configuration of the simulated P-band UWB BSAR experiment.

IV. EXPERIMENTAL RESULTS

In order to validate the proposed FFBP method for the reconstruction of the P-band UWB BSAR raw data, the experimental results based on the simulated and measured data are shown and analyzed. The simulated P-band UWB BSAR data of the scene containing several point-like scatterers and measured BSAR data acquired by the P-band UWB BSAR experiment are reconstructed by the proposed FFBP method and bistatic BP method.

A. SIMULATED DATA OF POINT-LIKES SCATTERERS

Fig.6 shows the geometric configuration of the simulated P-band UWB BSAR experiment including the motion errors. The parameters of the simulated P-band UWB BSAR experiment are shown in Table 1. The receiver ideal track is parallel to the Y axis, and the angle between the ideal track of the transmitter and the X axis is about $33.69°$. The transmitter and receiver positions at $\eta = 0$ are (x_{T0}, y_{T0}, z_{T0}) and (x_{R0}, y_{R0}, z_{R0}), respectively. For simplicity, we assume that the same motion error is added to the ideal tracks of both transmitter and receiver. The motion error in the X axis is $\delta_{Tx} = \delta_{Rx} = 4\sin(2\pi(1/T_a)\eta) + 0.2\eta$, the motion error in the Y axis is $\delta_{Ty} = \delta_{Ry} = \sin(2\pi(0.1/T_a)\eta) + 0.3\eta$, and the motion error in the Z axis is $\delta_{Tz} = \delta_{Rz} = 2\sin(2\pi(0.3/T_a)\eta) + 0.1\eta$. T_a is the synthetic aperture time in Table 1. The size of the simulated BSAR scene is 300m $\times$ 300m in range and azimuth, respectively. The scene contains nine point-like scatterers labeled as A~I in 3 rows and

TABLE 1. Parameters of the simulated P-band UWB BSAR experiment.

Parameter	Value	Parameter	Value
Carried frequency	600MHz	Synthetic aperture time	12.6s
Signal bandwidth	200MHz	Receiver ideal altitude	20m
Sampling frequency	300MHz	Receiver ideal speed	50m/s
PRF	100Hz	Transmitter ideal altitude	100m
Pulse duration	1us	Transmitter ideal speed	45m/s

3 columns, which are equally spaced in an area. Both the azimuth and range intervals of all point-like scatterers are 100m in the ground plane, and the RCS of all point-like scatterers are assumed to be 1 m^2. The point-like scatterer E is located at the center of the scene, i.e., (1650, 0, 0)m. The sampling intervals of the Cartesian BSAR image grid are assumed to be 0.8m in the azimuth and 0.6m in the range, respectively. Please note that, for the evaluation purpose, the effects of the radio frequency interference (RFI), jamming, clutter, noise, multi path, and local reflection are not considered in this paper.
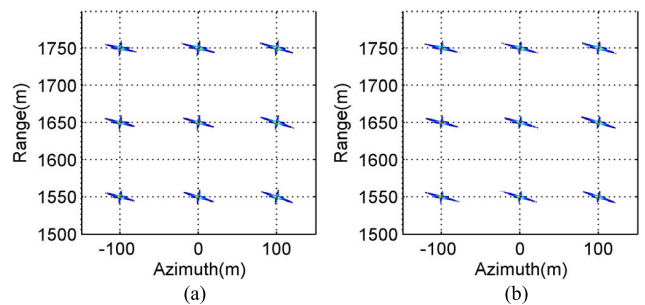

FIGURE 7. Reconstruction results of the simulated P-band UWB BSAR raw data. (a) Bistatic BP method; (b) Proposed FFBP method.

Fig.7 gives the reconstruction results of the simulated P-band UWB BSAR raw data by two methods. In Fig.7(a), all point-like scatterers in the simulated BSAR scene are well focused by the bistatic BP method, and appear like the points. In Fig.7(b), it can be found that the simulated BSAR scene can be also well reconstructed by the proposed FFBP method, and all point-like scatterers also appear like the points. It is seen that the focusing quality of all point-like scatterers in Fig.7(b) looks quite like that in Fig.7(a). Fig.8 shows the reconstruction results of the point-like scatterers E, I and A, which are extracted from Fig.7. Because the range and azimuth resolutions of the selected point-like scatterers is different, thus the scale of the images in the range and azimuth direction is different in Fig.8, in order to offer a clearer comparison of the focusing performance of selected point-like scatterers obtained by the two methods, both in the range and azimuth. In Fig.8(a), it can be found that the P-band UWB features of the selected point-like scatterers, such as the symmetrical, nonorthogonal and orthogonal sidelobes. However, it can be found that the azimuth nonorthogonal sidelobes of the selected point-like scatterers in the lower left and upper right are weaker than those in the upper left and lower right, which could be dependent on the BSAR geometric configuration, e.g., the angle between the tracks of the transmitter and receiver. In addition, it is found that the range sidelobes of the selected point-like scatterers are inclined with a certain angle, which may depend on the motion of the illuminating beam centers of the transmitter and receiver. In Fig.8(b), it is found that the reconstruction results of the selected point-like scatterers are very similar to those in Fig.8(a). Also, the typical P-band UWB feature
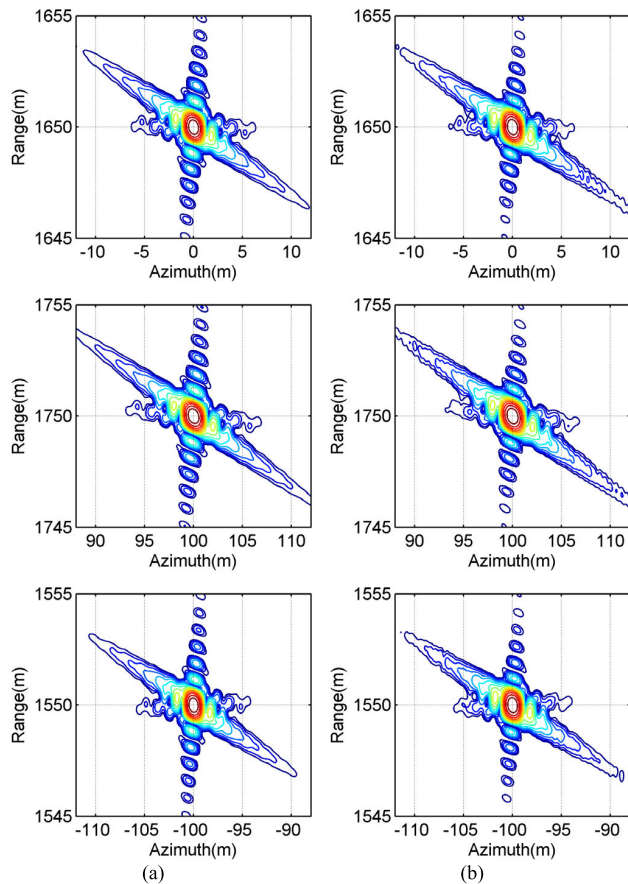
FIGURE 8. Contours of the reconstruction results of the point-like scatterers E, I and A in Fig.7. (a) Bistatic BP method; (b) Proposed FFBP method. Top row is the scatterer E, middle row is the scatterer I, and bottom row is the scatterer A.

FIGURE 9. Comparison between the reconstruction results by two methods for the point-like scatterer E. (a) Range amplitude; (b) Range phase; (c) Azimuth amplitude; (d) Azimuth phase.
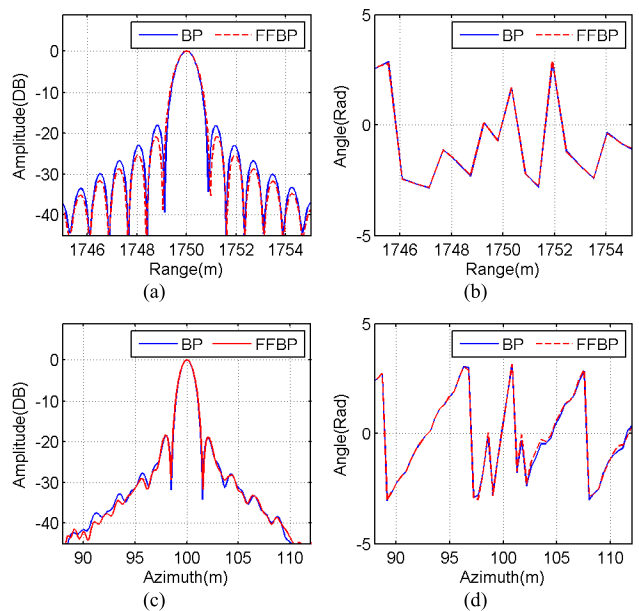
FIGURE 10. Comparison between the reconstruction results by two methods for the point-like scatterer I. (a) Range amplitude; (b) Range phase; (c) Azimuth amplitude; (d) Azimuth phase.

of the point-like scatterer illuminated by the P-band UWB BSAR can be also observed in Fig.8(b). Unfortunately, the reconstruction quality of the selected point-like scatterers in Fig.8(b) is slightly degraded with respect to those in Fig.8(a), since there may be little residual phase error caused by the approximate processing in the proposed FFBP method. Fortunately, the effect of the residual phase error is only small at the lower contour levels, while hardly visible at the high contour levels. That is to say, only the sidelobes of the point-like scatterers may slightly suffer from the effect of this phase errors.

To offer a more clear evaluation, the amplitude and phase profiles of the reconstruction results of the selected point-like scatterers in the azimuth and range are extracted from Fig.8, and plotted in Fig.9∼ Fig.11. From Fig.9∼ Fig.11, it is seen the amplitude and phase profiles of the reconstructed point-like scatterers by two methods are very similar. Properly speaking, in the mainlobe areas of the amplitude profiles, it is hardly possible to see the differences between two methods. However, in the sidelobe areas of the amplitude profiles, there is still slight difference between two methods, due to the effect of the residual phase errors in the proposed FFBP
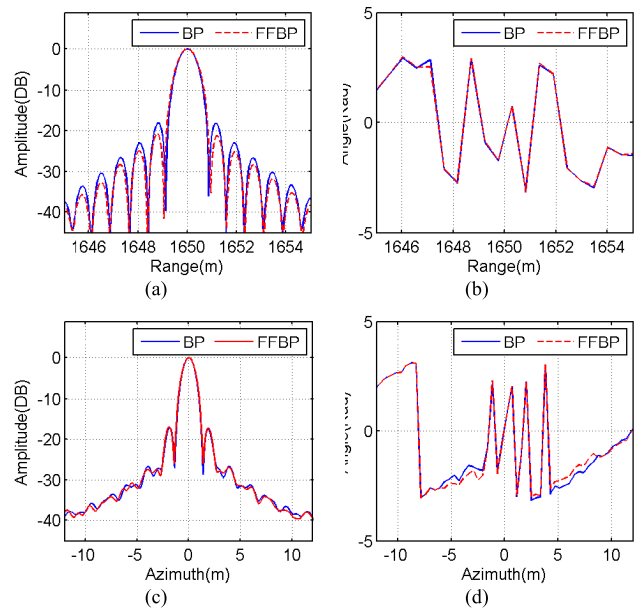
method. It is clearly found that the similar performance can be observed in the phase profiles for all selected point-like scatterers by two methods. It is hardly possible to see any difference in the mainlobes of the angle profiles (phase profiles) between two methods, while there is a slight difference in the sidelobes of angle profiles between two algorithms. Luckily, such influence of residual phase errors in the proposed FFBP method only degrades slightly the quality of the P-band UWB BSAR images.

FIGURE 11. Comparison between the reconstruction results by two methods for the point-like scatterer A. (a) Range amplitude; (b) Range phase; (c) Azimuth amplitude; (d) Azimuth phase.
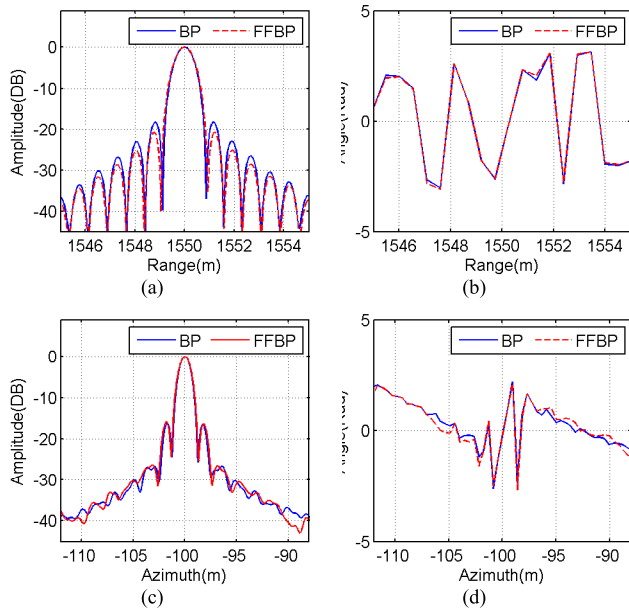
TABLE 2. Measured parameters of the selected point-like scatterers.

Methods	Measured parameters		Scatterer I	Scatterer E	Scatterer A
Bistatic BP method	Resolution (m)	Range	0.740	0.737	0.736
		Azimuth	1.238	1.146	1.061
	PSLR (dB)	Range	-18.16	-18.16	-16.15
		Azimuth	-16.54	-17.17	-18.20
	ISLR (dB)	Range	-16.45	-16.46	-16.46
		Azimuth	-16.51	-15.41	-14.68
Proposed FFBP method	Resolution (m)	Range	0.776	0.776	0.772
		Azimuth	1.269	1.187	1.125
	PSLR (dB)	Range	-18.89	-18.72	-15.87
		Azimuth	-17.41	-17.93	-18.77
	ISLR (dB)	Range	-17.27	-17.27	-17.14
		Azimuth	-16.72	-15.46	-14.51

In order to quantitatively analyze the performance of the proposed FFBP method, the measured parameters (i.e., the resolution, peak sidelobe ratio (PSLR) and integrated sidelobe ratio (ISLR)) of the P-band UWB BSAR image are calculated based on the amplitude profiles in Fig.9~ Fig.11, which are listed in Table 2. From Table 2, we can see that measured parameters by two methods are nearly the same. The PSLRs and ISLRs of the selected point-like scatterers by two methods are very similar. However, the resolutions of the selected point-like scatterers by the proposed FFBP method become little worse than those of the bistatic BP method, due to the effect of the residual phase errors in the proposed FFBP method.

Compared to the bistatic BP method, the efficiency improvement of the proposed FFBP method is decided by the reduction of the reconstruction time of the BSAR scene by the proposed FFBP method. Thus, the reconstruction time of two methods is measured on the same condition. They are

programmed and run in MATLAB on a Personal Computer with a 2.93 GHz Dual-Core Central Processing Unit and 2.00 GB Random Access Memory. Reconstruction time of the proposed FFBP method and bistatic BP method are 46.2s and 665.8s, respectively. Thus, the reconstruction efficiency of the proposed FFBP method, compared with the bistatic BP method, can be improved about 14.5 times, which corresponds with the theoretical results in Fig.5.

B. MEASURED DATA OF P-BAND UWB BSAR EXPERIMENT
To prove the applicability of the proposed FFBP method, the P-band UWB BSAR experiment has been conducted to acquire the measured BSAR data [51], which is processed by the two methods, and then the reconstruction results are shown and analyzed.
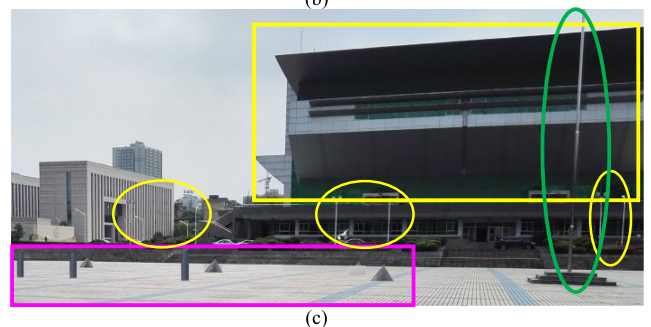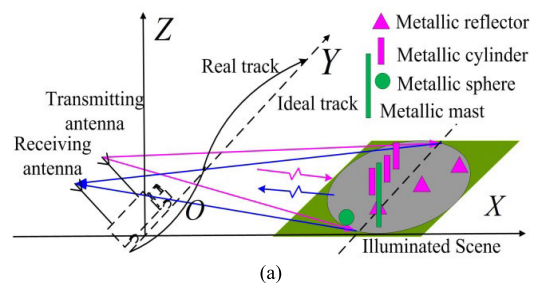

FIGURE 12. Along-track P-band UWB BSAR experiment. (a) Geometry; (b) Vehicle-based P-band UWB BSAR system; (c) Illuminated scene.

In the summer, a vehicle-based along track P-band UWB BSAR experiment has been conducted in China [51], which is shown in Fig.12. In Fig.12(a), the dashed line was the vehicle's ideal track, and the solid curve was its actual track. In Fig.12(b), P-band UWB BSAR system was integrated onboard an IVECO vehicle. The transmitting antenna was set on the right front of the vehicle's roof, and the receiving
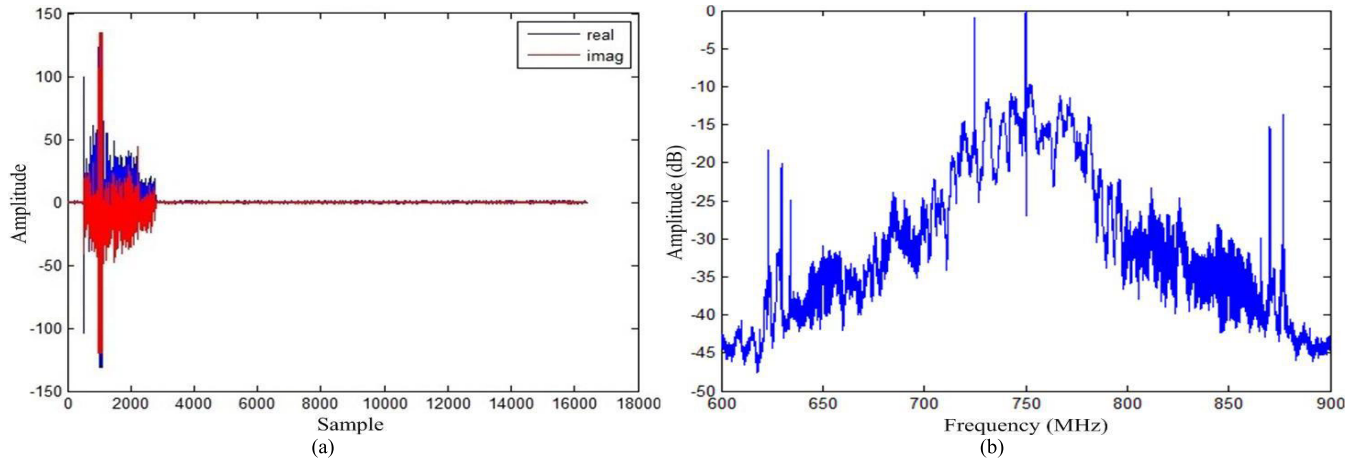
FIGURE 13. Bistatic raw data of the illuminated scene. (a) Bistatic raw data from one transmitted radar pulse, including the real (blue line) and imaginary (red line); (b) Sum of the frequency spectrum of the bistatic raw data from 100 radar pulses.

antenna has been set on the right rear of the vehicle's roof, which were arranged in a HH polarization [51]. Transmitter transmitted the chirp radar signal to the scene, whereas the receiver illuminated the same region and then received the scattered signal of the scene. The global positioning system (GPS) antenna was set on the middle of the vehicle's roof to record the vehicle position information. In Fig.12(c), the scene includes the triangle reflectors and cylinders (in the red rectangle), mast and sphere (in the green ellipse), street lamp (in the yellow ellipse), as well as the gymnasium (in the yellow rectangle). The positions of triangle reflectors are about (37.8, 38.8, 0)m, (48.2, 49.2, 0)m and (58.6, 59.6, 0)m, respectively. The positions of the cylinders are about (32.7, 46.6, 0)m, (32.7, 49.2, 0)m and (32.7, 51.8, 0)m, respectively. The mast's position is about (40, 31, 0)m.

TABLE 3. Parameters of the along-track P-band UWB BSAR experiment.

Parameter	Value	Parameter	Value
Signal frequency	P-band	Sampling frequency	300Hz
Polarization	HH	Pulse duration	200ns
PRF	1000Hz	Transmitter/receiver elevation angle	86.9°

The parameters of the along-track P-band UWB BSAR experiment is listed in Table 3. The vehicle moves along the Y axis with the speed about 3.5m/s. The initial positions of the transmitting and receiving antennas are about (0, 2, 4)m and (0, −2, 4)m. One data site was selected for the reconstruction: the scene is a flat area, which has the size about 110m in the X axis and 80m in the Y axis. The scene center is about (75, 40, 0)m. Fig.13 gives the bistatic raw data of the scene in the frequency domain and time domain. In Fig.13(a), the real (blue line) and imaginary (red line) components of the bistatic raw data is not complicated due to the geometric configuration. In Fig.13(b), we can see the raw data of the metallic targets in the frequency domain, since these metallic targets were deployed at the flat and open square, the power of their raw data is strong in theory.

To prove the feasibility of the proposed FFBP method, the vehicle-based along-track P-band UWB BSAR raw data is reconstructed by the bistatic BP method and proposed FFBP method, which is shown in Fig.14. From Fig.14, it is seen that the scene is well reconstructed by two methods, and the metallic targets as well as the gymnasium are well focused, the P-band UWB feature of the metallic targets can be clearly observed. Besides, it is found that the BSAR image in Fig.14(b) by the proposed FFBP method is very similar to the BSAR image in Fig.14(a) by the bistatic BP method. However, the reconstruction quality of the BSAR image in Fig.14(b) is slightly degraded compared with that of the BSAR image in Fig.14(a), since there may be still residual phase error in the proposed FFBP method.

To quantitatively evaluate the reconstruction quality of the BSAR images in Fig.14, the resolutions and PSLRs in the X and Y axes of the focused triangle reflector and cylinder in the yellow circles in Fig.14 are measured, and then listed in Table 4. From Table 4, it can be found that the measured parameters by two methods are very similar, which proves the validity of the proposed FFBP method.

TABLE 4. Measured parameters of the selected reflector and cylinder.

Methods	Measured parameters		Reflector	Cylinder
Bistatic BP method	Resolution (m)	X axis	1.820	1.148
		Y axis	0.227	0.185
	PSLR (dB)	X axis	−5.90	−8.16
		Y axis	−13.21	−13.17
Proposed FFBP method	Resolution (m)	X axis	1.852	1.157
		Y axis	0.301	0.219
	PSLR (dB)	X axis	−5.89	−8.20
		Y axis	−10.01	−13.26

The reconstruction time of the scene using the bistatic BP method is about 23028s, while the reconstruction time of the scene using proposed FFBP method is about 2123s. Compared with the bistatic BP method, the reconstruction efficiency of the proposed FFBP method is improved about 10.8 times, which shows that it is able to satisfy
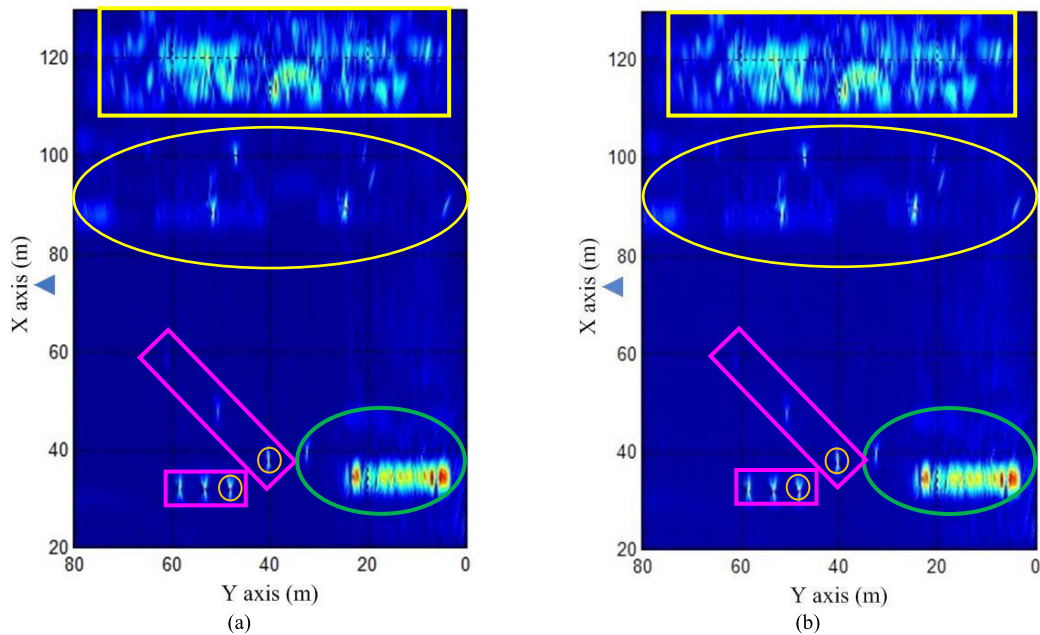
FIGURE 14. Reconstruction results of the vehicle-based along-track P-band UWB BSAR raw data. (a) Bistatic BP method; (b) Proposed FFBP method.

the high-efficiency and high-precision reconstruction of the P-band UWB BSAR raw data in reality.

V. CONCLUSION

This paper presents a high-efficiency and high-precision reconstruction strategy for the P-band UWB BSAR raw data of the huge amount, large spatial-variance, significant range-azimuth coupling and complicated motion error. This method requires the local beamforming from the raw data as an the intermediate processing in the slant range plane instead of the ground plane, to be exactly referenced to the tracks of the transmitter and receiver considering platform altitudes. And, it derives the requirement for selecting the subapertures and subimages by analyzing the bistatic range error considering the motion errors, as well as the sampling requirement of the beam for the subimages, to offer a near-optimum tradeoff between the reconstruction efficiency and precision. The proposed reconstruction strategy has been verified by the simulated and measured P-band UWB BSAR raw data, which confirms that this proposed strategy is effective, and can achieve the near optimal performance with a low computational complexity. In the future works, we would like to focus on the detection, identification and classification of the concealed targets by the P-band UWB BSAR system, and then the more extensive P-band UWB BSAR experiment with the different operation modes will be carried out, and then the corresponding data processing strategy will be studied.

ACKNOWLEDGMENT

REFERENCES

[1] Y. Wang, Z. Dong, and Y. Zhu, "Multiscale block fusion object detection method for large-scale high-resolution remote sensing imagery," *IEEE Access*, vol. 7, pp. 99530–99539, 2019.

[2] Z. Liu, L. Wang, X. Wang, X. Shen, and L. Li, "Secure remote sensing image registration based on compressed sensing in cloud setting," *IEEE Access*, vol. 7, pp. 36516–36526, 2019.

[3] Y. Li and D. Ye, "Greedy annotation of remote sensing image scenes based on automatic aggregation via hierarchical similarity diffusion," *IEEE Access*, vol. 6, pp. 57376–57388, 2018.

[4] L. Wang, "Multi-frequency holographic microwave imaging for breast lesion detection," *IEEE Access*, vol. 7, pp. 83984–83993, 2019.

[5] K. Zhang, K. Yang, S. Li, and H.-B. Chen, "A difference-based local contrast method for infrared small target detection under complex background," *IEEE Access*, vol. 7, pp. 105503–105513, 2019.

[6] P. Du, S. Zhang, C. Chen, H. Yang, W.-D. Zhong, R. Zhang, A. Alphones, and Y. Yang, "Experimental demonstration of 3D visible light positioning using received signal strength with low-complexity trilateration assisted by deep learning technique," *IEEE Access*, vol. 7, pp. 93986–93997, 2019.

[7] K.-Y. Chen, H.-T. Vu, C.-C. Yang, C.-C. Hsu, and Y.-K. Su, "Amorphous MgInO ultraviolet solar-blind photodetectors," *IEEE Access*, vol. 7, pp. 103250–103254, 2019.

[8] L. Yu, Q. Yang, and L. Dong, "Aircraft target detection using multimodal satellite-based data," *Signal Process.*, vol. 155, pp. 358–367, Feb. 2019.

[9] C. Wen, M. Tao, J. Peng, J. Wu, and T. Wang, "Clutter suppression for airborne FDA-MIMO radar using multi-waveform adaptive processing and auxiliary channel STAP," *Signal Process.*, vol. 154, pp. 280–293, Jan. 2019.

[10] J. Liu, J. Han, Z.-J. Zhang, and J. Li, "Target detection exploiting covariance matrix structures in MIMO radar," *Signal Process.*, vol. 154, pp. 174–181, Jan. 2019.

[11] M. Bolhasani, E. Mehrshahi, S. A. Ghorashi, and M. S. Alijani, "Constant envelope waveform design to increase range resolution and SINR in correlated MIMO radar," *Signal Process.*, vol. 163, pp. 59–65, Oct. 2019.

[12] M. Miltiadou, N. D. Campbell, S. Gonzalez Aracil, T. Brown, and M. G. Grant, "Detection of dead standing Eucalyptus camaldulensis without tree delineation for managing biodiversity in native Australian forest," *Int. J. Appl. Earth Observ. Geoinf.*, vol. 67, pp. 135–147, May 2018.

[13] S. Homayouni, H. Mcnairn, M. Hosseini, X. Jiao, and J. Powers, "Quad and compact multitemporal C-band PolSAR observations for crop characterization and monitoring," *Int. J. Appl. Earth Observ. Geoinf.*, vol. 74, pp. 78–87, Feb. 2019.

[14] J. Li, S. Wang, G. Gunn, P. Joosse, and H. A. Russell, "A model for downscaling SMOS soil moisture using Sentinel-1 SAR data," *Int. J. Appl. Earth Observ. Geoinf.*, vol. 72, pp. 109–121, Oct. 2018.

[15] J. Van Der Sanden, N. Short, and H. Drouin, "InSAR coherence for automated lake ice extent mapping: TanDEM-X bistatic and pursuit mono-static results," *Int. J. Appl. Earth Observ. Geoinf.*, vol. 73, pp. 605–615, Dec. 2018.

[16] M. Abdelkareem, G. M. Kamal El-Din, and I. Osman, "An integrated approach for mapping mineral resources in the eastern desert of egypt," *Int. J. Appl. Earth Observ. Geoinf.*, vol. 73, pp. 682–696, Dec. 2018.

[17] E. Fiorillo, F. Maselli, V. Tarchiani, and P. Vignaroli, "Analysis of land degradation processes on a tiger bush plateau in South West Niger using MODIS and LANDSAT TM/ETM+ data," *Int. J. Appl. Earth Observ. Geoinf.*, vol. 62, pp. 56–68, Oct. 2017.

[18] M. Liu, X. Liu, B. Zhang, and C. Ding, "Regional heavy metal pollution in crops by integrating physiological function variability with spatio-temporal stability using multi-temporal thermal remote sensing," *Int. J. Appl. Earth Observ. Geoinf.*, vol. 51, pp. 91–102, Sep. 2016.

[19] P. Addison and T. Oommen, "Utilizing satellite radar remote sensing for burn severity estimation," *Int. J. Appl. Earth Observ. Geoinf.*, vol. 73, pp. 292–299, Dec. 2018.

[20] J. Yang, T. Jin, and X. Huang, "Compressed sensing radar imaging with magnitude sparse representation," *IEEE Access*, vol. 7, pp. 29722–29733, 2019.

[21] M. G. Fernandez, Y. A. Lopez, A. A. Arboleya, B. G. Valdes, Y. R. Vaqueiro, F. Las-Heras Andres, and A. P. Garcia, "Synthetic aperture radar imaging system for landmine detection using a ground penetrat-ing radar on board a unmanned aerial vehicle," *IEEE Access*, vol. 6, pp. 45100–45112, 2018.

[22] X. Ye, F. Zhang, Y. Yang, D. Zhu, and S. Pan, "Photonics-based high-resolution 3d inverse synthetic aperture radar imaging," *IEEE Access*, vol. 7, pp. 79503–79509, 2019.

[23] H. Hellsten, S. Sahlin, and P. Dammert, "Polarimetric subsurface SAR imaging outcome of theoretical development and CARABAS III tests," in *Proc. Int. Radar Conf. (RADAR)*, Lille, France, Oct. 2014, pp. 601–606.

[24] D. An, X. Huang, T. Jin, and Z. Zhou, "Extended two-step focusing approach for squinted spotlight SAR imaging," *IEEE Trans. Geosci. Remote Sens.*, vol. 50, no. 7, pp. 2889–2900, Jul. 2012.

[25] H. T. Xie, D. X. An, X. T. Huang, and Z. M. Zhou, "Research on spatial resolution of one-stationary bistatic ultrahigh frequency ultrawidebeam ultrawideband SAR," *IEEE J. Sel. Topics Appl. Earth Observ. Remote Sens.*, vol. 8, no. 4, pp. 1782–1798, Apr. 2015.

[26] M. Soumekh, *Synthetic Aperture Radar Signal Processing: With MATLAB Algorithms*. Hoboken, NJ, USA: Wiley, 1999.

[27] M. Rodriguez-Cassola, S. V. Baumgartner, G. Krieger, and A. Moreira, "Bistatic TerraSAR-X/F-SAR spaceborne-airborne SAR experiment: Description, data processing, and results," *IEEE Trans. Geosci. Remote Sens.*, vol. 48, no. 8, pp. 781–794, Feb. 2010.

[28] D. X. An, "Bistatic P band UWB SAR experiment and raw data pro-cessing," in *Proc. CIE Int. Conf. Radar*, Guangzhou, China, Oct. 2016, pp. 356–359.

[29] I. Walterscheid, T. Espeter, A. Brenner, J. Klare, J. Ender, H. Nies, R. Wang, and O. Loffeld, "Bistatic SAR experiments with PAMIR and TerraSAR-X-setup, processing, and image results," *IEEE Trans. Geosci. Remote Sens.*, vol. 48, no. 8, pp. 3268–3279, Aug. 2010.

[30] M. Rodriguez-Cassola, "First bistatic SAR experiments with TanDEM-X," *IEEE Geosci. Remote Sens. Lett.*, vol. 9, no. 1, pp. 33–37, Jan. 2012.

[31] D. Gromek, K. Kulpa, and P. Samczynski, "Experimental results of passive SAR imaging using DVB-T illuminators of opportunity," *IEEE Geosci. Remote Sens. Lett.*, vol. 13, no. 8, pp. 1124–1128, Aug. 2016.

[32] A. Amini, P. M. Esfahani, M. Ghavami, and F. Marvasti, "UWB orthogo-nal pulse design using Sturm-Liouville boundary value problem," *Signal Process.*, vol. 159, pp. 147–158, Jun. 2019.

[33] L. M. H. Ulander, M. J. Soja, A. Gustavsson, E. Blomberg, and J. E. S. Fransson, "Mono- and bistatic UHF-band SAR measurements of a hemi-boreal forest," in *Proc. IEEE Int. Geosci. Remote Sens. Symp. (IGARSS)*, Milan, Italy, Jul. 2015, pp. 5079–5082.

[34] L. M. H. Ulander, A. Gustavsson, T. Jonsson, R. Ragnarsson, and G. Stenström, "Development of CARINA bistatic VHF-band SAR," in *Proc. Int. Radar Conf. (RADAR)*, Lille, France, Oct. 2014, pp. 601–606.

[35] L. N. Yew, F. H. Wong, and I. G. Cumming, "Processing of azimuth invariant bistatic SAR data using the range Doppler algorithm," *IEEE Trans Geosci Remote Sens.*, vol. 46, no. 1, pp. 14–21, 2008.

[36] Y. Li, Z. Zhang, M. Xing, and Z. Bao, "Bistatic spotlight SAR processing using the frequency-scaling algorithm," *IEEE Geosci. Remote Sens. Lett.*, vol. 5, no. 1, pp. 48–52, Jan. 2008.

[37] X. Qiu, D. Hu, and C. Ding, "An omega-K algorithm with phase error compensation for bistatic SAR of a translational invariant case," *IEEE Trans. Geosci. Remote Sens.*, vol. 46, no. 8, pp. 2224–2232, Aug. 2008.

[38] Y. P. Wang, W. X. Tan, W. Hong, Y. Lin, and Y. R. Wu, "Focusing bistatic circular SAR data using polar format algorithm," in *Proc. Asia–Pacific Conf. Synth. Aperture Radar (APSAR)*, Xi'an, China, Oct. 2009, pp. 989–992.

[39] R. Wang, O. Loffeld, H. Nies, S. Knedlik, and J. Ender, "Chirp-scaling algorithm for bistatic SAR data in the constant-offset configuration," *IEEE Trans. Geosci. Remote Sens.*, vol. 47, no. 3, pp. 952–964, Dec. 2009.

[40] F. Wong, I. Cumming, and Y. Lam Neo, "Focusing bistatic SAR data using the nonlinear chirp scaling algorithm," *IEEE Trans. Geosci. Remote Sens.*, vol. 46, no. 9, pp. 2493–2505, Sep. 2008.

[41] J. L. Bauck and W. K. Jenkins, "Convolution-backprojection image recon-struction for bistatic synthetic aperture radar," in *Proc. IEEE Int. Symp. Circ. Syst. (ISCAS)*, Portland, OR, USA, Jul. 1989, pp. 631–634.

[42] L. M. H. Ulander, B. Flood, P.-O. Frölind, T. Jonsson, A. Gustavsson, J. Rasmusson, G. Stenström, A. Barmettler, and E. Meier, "Bistatic exper-iment with ultra-wideband VHF-band synthetic-aperture radar," in *Proc. Eur. Symp. Synth. Aperture Radar (EUSAR)*, Friedrichshafen, Germany, Jul. 2008, pp. 1–4.

[43] L. M. H. Ulander, P.-O. Frölind, A. Gustavsson, D. Murdin, and G. Stenström, "Fast factorized back-projection for bistatic SAR pro-cessing," in *Proc. Eur. Symp. Synth. Aperture Radar (EUSAR)*, Aachen, Germany, Jun. 2010, pp. 1002–1005.

[44] M. Rodriguez-Cassola, P. Prats, G. Krieger, and A. Moreira, "Efficient time-domain image formation with precise topography accommodation for general bistatic SAR configurations," *IEEE Trans. Aerosp. Electron. Syst.*, vol. 47, no. 4, pp. 2949–2966, Oct. 2011.

[45] H. Xie, D. An, X. Huang, and Z. Zhou, "Fast time-domain imaging in elliptical polar coordinate for general bistatic VHF/UHF ultra-wideband SAR with arbitrary motion," *IEEE J. Sel. Topics Appl. Earth Observ. Remote Sens.*, vol. 8, no. 2, pp. 879–895, Feb. 2015.

[46] V. T. Vu and M. I. Pettersson, "Fast backprojection algorithms based on subapertures and local polar coordinates for general bistatic air-borne SAR systems," *IEEE Trans. Geosci. Remote Sens.*, vol. 54, no. 5, pp. 2706–2712, May 2016.

[47] V. T. Vu and M. I. Pettersson, "Nyquist Sampling requirements for polar grids in bistatic time-domain algorithms," *IEEE Trans. Signal Process.*, vol. 63, no. 2, pp. 457–465, Jan. 2015.

[48] V. T. Vu, T. K. Sjogren, and M. I. Pettersson, "Fast time-domain algorithms for UWB bistatic SAR processing," *IEEE Trans. Aerosp. Electron. Syst.*, vol. 49, no. 3, pp. 1982–1994, Jul. 2013.

[49] H. Xie, S. Shi, F. Li, D. An, H. Xiao, C. Xie, Q. Fang, G. Wang, L. Wang, F. Wang, G. Wang, X. Hang, and Z. Zhou, "Fast time domain approach for bistatic forward-looking SAR imaging based on subaperture processing and local beamforming," in *Proc. Int. Conf. Frontiers Sensors Technol.*, ShenZhen, China, Apr. 2017, pp. 240–245.

[50] L. Ulander, H. Hellsten, and G. Stenström, "Synthetic-aperture radar processing using fast factorized back-projection," *IEEE Trans. Aerosp. Electron. Syst.*, vol. 39, no. 3, pp. 760–776, Jul. 2003.

[51] H. T. Xie, S. Shi, J. Mao, F. Li, D. An, Z. Zhou, and G. Wang, "Exper-iment of azimuth-invariant bistatic UHF UWB SAR," in *Proc. Int. Conf. Commun., Image Signal Process.*, Shenzhen, China, Nov. 2017, pp. 1–5.

HONGTU XIE (Member, IEEE) was born in 1986. He received the B.S. degree in electronic infor-mation engineering from Hunan University, Changsha, China, in 2008, and the M.S. degree in electronic science and technology and the Ph.D. degree in information and communication engi-neering from the National University of Defense Technology (NUDT), Changsha, in 2010 and 2015, respectively.

He is currently an Associate Professor and a M.S. Supervisor with the School of Electronics and Communication Engi-neering, Sun Yat-sen University (SYSU), Guangzhou, China, and a judge's expert of the National Natural Science Foundation of China. His research field is the advanced radar system and technology, including the low fre-quency ultra-wideband SAR imaging, and target detection and recognition.

Dr. Xie received the Excellent Doctoral Dissertation of Chinese People's Liberation Army Award for his Ph.D. dissertation, in 2018.

JUN HU (Member, IEEE) received the B.S. degree in electronic information engineering from Hunan University, Changsha, China, in 2008, and the M.S. degree in electronic science and technology and the Ph.D. degree in information and communication engineering from the National University of Defense Technology, Changsha, in 2010 and 2015, respectively.

He is currently a Lecturer and a M.S. Supervisor with the School of Electronics and Communication Engineering, Sun Yat-sen University, Guangzhou, China. His research field is the advanced radar system and technology, including the radar imaging, and target detection and recognition.

KEQING DUAN (Member, IEEE) received the B.S. and M.S. degrees from the Wuhan Early Warning Academy, Wuhan, China, and the Ph.D. degree from the National University of Defense Technology, Changsha, China, in 2003, 2006, and 2010, respectively, all in electrical engineering.

He is currently an Associate professor and a M.S. Supervisor with the School of Electronics and Communication Engineering, Sun Yat-sen University, Guangzhou, China. His research interests include the array signal processing, space-time adaptive processing, compressive sensing, and its application to radar systems.

GUOQIAN WANG received the B.S. degree in clinical medicine of the traditional Chinese medicine and western medicine and the M.S. degree in internal medicine of the traditional Chinese medicine from the Hunan University of Traditional Chinese Medicine, Changsha, China, in 2010 and 2015, respectively.

She is currently a Physician with the Sun Yat-sen Memorial Hospital, Sun Yat-sen University, Guangzhou, China. Her research interests include cardiology, cardiography, and medical diagnostic imaging.

● ● ●